Preprint Title Nanoscale capacitance spectroscopy based on multi-frequency electrostatic force microscopy

Authors Pascal N. Rohrbeck, Lukas D. Cavar, Franjo Weber, Peter G. Reichel, Mara Niebling and Stefan A. L. Weber

Publication Date 20 Dez. 2024

Article Type Full Research Paper

Supporting Information File 1 H-SCM Publication SI.zip; 64.2 MB

ORCID® iDs Pascal N. Rohrbeck - https://orcid.org/0000-0002-1514-6008

Nanoscale capacitance spectroscopy based on multi-frequency electrostatic force microscopy

Pascal N. Rohrbeck[1,2], Lukas D. Cavar[1,3], Franjo Weber[1,2], Peter G. Reichel[1], Mara Niebling[1,3] and Stefan A. L. Weber*[1,3,4]

Address: [1]Max Planck Institute for Polymer Research, Ackermannweg 10, 55128 Mainz, Germany; [2]Department of Chemistry, University of Mainz, Duesbergweg 10-14, 55128 Mainz, Germany; [3]Department of Physics, University of Mainz, Staudingerweg 7, 55128 Mainz, Germany and [4]Institute for Photovoltaics, University of Stuttgart, Pfaffenwaldring 47, 70569 Stuttgart, Germany

Email: Stefan A. L. Weber - stefan.weber@mpip-mainz.mpg.de; Stefan.Weber@ipv.uni-stuttgart.de

* Corresponding author

Abstract

We present Heterodyne Scanning Capacitance Microscopy (H-SCM) as a novel multi-frequency electrostatic force microscopy method for nanoscale capacitance characterization. Next to a high spatial resolution, the key advantage of the multi-frequency approach of H-SCM is that it allows for operation at almost arbitrary frequencies, enabling the measurement of the local dielectric function over a wide range of frequencies. We demonstrate the reliable operation of H-SCM using standard Atomic Force Microscopy (AFM) equipment plus an external lock-in amplifier up to a frequency of 5 MHz. Our results show a significant reduction of signal background, resulting in higher locality of the measurements with less cross-talk. Combined with improved models for the tip-sample capacity, H-SCM will pave the way for quantitative studies of dielectric effects in nanoscale systems in materials science, biology, and nanotechnology.

Keywords

Atomic force microscopy; capacity gradients; dielectric constant; dielectric spectroscopy; hetero-

dyne frequency mixing; Kelvin Probe Force Microscopy; quantitative force spectroscopy; scanning capacitance microscopy; multi frequency AFM;

Introduction

Technological progress in fields including electronics, energy storage, photonics, and biomedical devices would not have been possible without the development of new materials. Progress in these areas requires a detailed understanding of material properties, particularly at the nanoscale, where phenomena such as quantum confinement, interface effects, and defect dynamics play a critical role. Innovations in characterization techniques have enabled researchers to explore these properties with unprecedented precision, paving the way for the design of materials with tailored functionalities[1-6].

Dielectric properties are fundamental for understanding the behavior and performance of various material systems, as they directly influence charge storage, polarization, and energy dissipation mechanisms. For instance, in microelectronic devices, high-κ dielectric materials such as HfO_2 and ZrO_2 are critical for minimizing leakage currents and enhancing gate capacitance in transistors[7-9]. In energy storage systems, the dielectric constants of polymer-ceramic composites determine the efficiency and reliability of capacitors[10]. Similarly, in next-generation photovoltaic devices, the dielectric properties of absorber layers, such as lead-halide perovskites, affect carrier recombination and electric field distribution, thereby influencing power conversion efficiency[11].

At the nanoscale, the importance of dielectric properties becomes even more pronounced. Many advanced materials exhibit nanoscale structural heterogeneity, where quantum confinement, phase composition, and interfacial effects cause significant deviations in dielectric behavior compared to bulk materials[12,13]. These nanoscale variations influence key properties such as charge transport, polarization dynamics, and defect distributions, directly impacting the performance of microelectronic and energy systems[14,15]. Understanding these effects requires correlating nanoscale dielectric properties with structural and morphological features.

Scanning probe techniques have revolutionized nanoscale material characterization. Since the invention of Scanning Tunneling Microscopy (STM)[16] and Atomic Force Microscopy (AFM)[17], various electric force-based methods have emerged to study materials like perovskite solar cells[18-20] and Li-ion batteries[21-23]. AFM enables simultaneous acquisition of topographic and electronic data by applying AC or DC voltages across the tip-sample gap, allowing the detection of capacitive forces[24,25] or contact potential difference (CPD)[18]. Its exceptional spatial resolution, ranging from sub-micron[24,26] to atomic scales[27,28], makes AFM a powerful tool for nanoscale analysis.

Scanning capacitance microscopy (SCM) is another widely used technique for capacitance measurements. SCM quantifies intrinsic material properties, such as film thickness[29,30] and dielectric constants[30,31], with superior spatial resolution compared to conventional methods like ellipsometry or reflectance spectroscopy[30]. However, existing techniques face limitations due to nonlocal stray capacitances[32] and reliance on external cables and sensors, which compromise measurement accuracy and resolution[33,34].

To address these challenges, we present a novel, multi-frequency AFM-based method for nanoscale capacitance characterization. Our approach measures the second capacitance gradient $\left(\propto \frac{\partial^2 C}{\partial z^2}\right)$, enhancing localization by minimizing stray capacitance contributions[35]. This method enables high-frequency capacitance gradient spectroscopy without requiring specialized equipment beyond a lock-in amplifier.

The following sections introduce the theoretical framework of multi-frequency Electrostatic Force Microscopy (EFM), demonstrate its resolution enhancement experimentally, and validate its spectroscopic capabilities by measuring nanoscale dielectric properties of microfabricated SiO_2 samples. Finally, we compare its performance with established techniques through capacitance imaging of a Perfluoroalkyl-Alkane $F(CF_2)_{14}(CH_2)_{20}H$ (F14H20) sample.

Theory

Multi-frequency Electrostatic Force Microscopy

The electrostatic force F_{ES} between tip and sample can be understood in terms of the gradient of the energy, W_C, stored in the tip-sample capacitor C with respect to the tip-sample separation z, as given by

$$F_{ES} = \frac{\partial W_C}{\partial z} = \frac{1}{2} \cdot \frac{\partial C}{\partial z} \cdot V^2_{\text{tip-sample}}, \tag{1}$$

where $V_{\text{tip-sample}}$ specifies the electrical voltage across the tip-sample gap. In conventional EFM with single-frequency excitation, $V_{\text{tip-sample}}$ is given by eq. (2).

$$V_{ES} = V_{DC} - V_{CPD} + V_{AC} \cdot \sin(\omega_e \cdot t)[18]. \tag{2}$$

with V_{DC} the direct current (DC)-Voltage offset applied to the tip, V_{AC} the alternating current (AC) voltage amplitude with the frequency ω_{AC} at a certain time t and V_{CPD} the contact potential difference (CPD), which corresponds to the difference in tip and sample work function[18]. Inserting equation eq. (2) into equation eq. (1), we obtain the following expression:

$$F_{ES} = \frac{1}{2}\frac{\partial C}{\partial z}\left((V_{DC} - V_{CPD})^2 + \frac{V^2_{AC}}{2}\right) \tag{3a}$$

$$+ \frac{\partial C}{\partial z}\,(V_{DC} - V_{CPD})\; V_{AC}\sin(\omega_e\, t) \tag{3b}$$

$$+ \frac{\partial C}{\partial z}\,\frac{V^2_{AC}}{4}\cos(2\,\omega_e\, t) \tag{3c}$$

Alongside a static component in eq. (3a), the electrostatic force has periodic time-dependent components at frequencies ω_e and $2\omega_e$ which corresponds to eqs. (3b) and (3c), respectively. In the case of an oscillating AFM tip, the tip-sample distance z and thereby the tip-sample capacitance and its gradients is changing periodically. This periodic fluctuation of the capacity gradient $C'(t) = \frac{\partial C}{\partial z}(t)$ adds an additional dynamic component to eq. (3). Using a Fourier expansion for the capacitance gradient $C'(t) = \frac{\partial C}{\partial z}(t)$ yields[18]:

$$C'(t) = C'(z_0) + C''(z_0) \cdot A_\mathrm{m} \cdot \cos(\omega_\mathrm{m} t) + \ldots \tag{4}$$

By inserting eq. (4) into eq. (3), we find that frequency mixing between $C'(t)$ and the electrostatic excitation leads to sidebands at frequencies $\omega_{\mathrm{SB},1} = (\omega_\mathrm{m} \pm \omega_\mathrm{AC})$ and $\omega_{\mathrm{SB},2} = (\omega_\mathrm{m} \pm 2\omega_\mathrm{AC})$ next to the the mechanical oscillation at ω_m[18]. The amplitude of the first harmonic frequency components is used in conventional amplitude modulation (AM) and sideband or heterodyne Kelvin Probe Force Microscopy (KPFM)[18]. The second harmonic signals are proportional to the local capacity gradients, providing information about the local tip-sample capacitance. To ensure a sufficient signal-to-noise ratio, the resulting frequencies should coincide with one of the cantilever's resonance frequencies, limiting the choice of excitation frequencies.

We can avoid this limitation by using a multi-frequency excitation approach. With a double-frequency excitation, we can write the tip-sample voltage as

$$V_\text{tip-sample} = V_{\mathrm{AC},1} \cdot \sin\left(\omega_{\mathrm{e},1}\right) + V_{\mathrm{AC},2} \cdot \sin\left(\omega_{\mathrm{e},2}\right) \tag{5}$$

In the case of two drives with identical amplitude $V_{\mathrm{AC},1} = V_{\mathrm{AC},2} = \frac{V_\mathrm{AC}}{2}$, eq. (5) can be rearranged as

$$V_\text{tip-sample} = V_\mathrm{AC} \cdot \sin\left(\frac{\omega_{\mathrm{e},1} - \omega_{\mathrm{e},2}}{2} t\right) \cdot \sin\left(\frac{\omega_{\mathrm{e},1} + \omega_{\mathrm{e},2}}{2} t\right). \tag{6}$$

Thus, the waveform can be viewed as a high-frequency oscillation at $(\omega_{\mathrm{e},1} + \omega_{\mathrm{e},2})/2$ with a low-frequency amplitude modulation at frequency $(\omega_{\mathrm{e},1} - \omega_{\mathrm{e},2})/2 = \Delta\omega_\mathrm{e}/2$. This effect is also known as "beating" and is utilized in the AFM context for example in intermodulation AFM[36-39].

By inserting eq. (4) and eq. (6) in eq. (3), we obtain the full expression for the electrostatic force.

Here, we will focus on the DC force component in eq. (3a) and set $V_{\mathrm{DC}} - V_{\mathrm{CPD}} = \Delta$:

$$F_{\mathrm{DC}} = \frac{1}{2}\left(C' + C'' A_{\mathrm{m}} \sin(\omega_{\mathrm{m}} t) + \dots\right) \cdot \left[\Delta^2 + \frac{V_{\mathrm{AC}}^2}{2} \sin^2(\Delta\omega_{\mathrm{e}}/2t)\right]$$

$$= \frac{1}{2}C' \left[\Delta^2 + \frac{V_{\mathrm{AC}}^2}{4}\right] + \frac{1}{8}C' V_{\mathrm{AC}}^2 \cos(\Delta\omega_{\mathrm{e}} t) \tag{7a}$$

$$+ \frac{1}{2}C'' A_{\mathrm{m}} \left[\Delta^2 + \frac{V_{\mathrm{AC}}^2}{4}\right] \sin(\omega_{\mathrm{m}} t) + \frac{1}{16}C'' A_{\mathrm{m}} V_{\mathrm{AC}}^2 \sin((\omega_{\mathrm{m}} \pm \Delta\omega_{\mathrm{e}} t) \tag{7b}$$

In addition to a static force term identical to eq. (3a), eq. (7a) contains a term proportional to C' at frequency $2\omega_{\mathrm{mod}} = \Delta\omega$. This force has been used for AM based dielectric spectroscopy[31,40-46]. The second term eq. (7b) contains a force component at the mechanical drive frequency ω_{m} and at a sideband frequency $\omega_{\mathrm{m}} \pm 2\omega_{\mathrm{mod}}$. The latter one is independent of of the local CPD, making it interesting for dielectric measurements. As the magnitude of this force component depends on C'', we can expect a superior lateral resolution through a reduction of long-ranged force contributions from tip cone and cantilever. As in the case of conventional EFM, signal-to-noise is greatly improved by choosing $\Delta\omega_{\mathrm{e}}$ such that one of the induced sidebands falls on one of the cantilever's mechanical resonances. We call this method heterodyne Scanning Capacitance Microscopy (H-SCM). To calculate the second capacitance gradient, we need to calculate the electrostatic force from the detected amplitude signal, A_{det}, taking into account the cantilever's frequency-dependent spring constant or transfer function, $k(\omega)$.

$$\frac{\partial^2 C}{\partial z^2} = C'' = \frac{16\, A_{\mathrm{det}} \cdot k(\omega)}{A_{\mathrm{m}} \cdot V_{\mathrm{AC}}^2} \tag{8}$$

Interestingly, the forces in eq. (7b) are only dependent on the frequency difference, $\Delta\omega_{\mathrm{e}}$, of the electrical drive frequencies. Thus, the experiments can be performed at almost arbitrarily high AC frequencies. The lower limit for the frequency range is given by the second resonance of the cantilever. Towards higher frequencies, the impedance of the electrical connection will introduce a damping of the excitation signal that has to be considered in eq. (8). By using appropriate means of coupling the electrical excitation into the tip-sample gap, experiments at microwave or even at optical frequencies are possible. In our setup, the two excitation frequencies can be varied in frequency from $\approx$ 600 kHz up to at least 50 MHz, limited by the bandwidth of the lock-in amplifier. To reach a nanoscale sensitive measurement of the dielectric constant in media besides air, a detection at higher excitation frequencies in the MHz regime is strictly necessary[47].

The indirect detection of local capacity variations by means of an electrstatic force has the advantage that it does not require additional devices for the measurement except for the lock-in amplifier (LIA) similar to the work of Gramse et al.[48]. Nevertheless, to quantify the total tip-sample capacitance will require varying the distance, e.g. by force-distance spectroscopy.

Methods

Heterodyne Scanning Capacitance Microscopy (H-SCM) to measure the second capacitive gradient C''

We perform heterodyne Scanning Capacitance Microscopy (H-SCM) using a conductive AFM cantilever in tapping mode with a mechanical drive near the fundamental cantilever eigenmode $\omega_{\mathrm{m},1}$ with a mechanical amplitude A_{m}. Additionally, we apply two high-frequency electrical excitations of identical magnitude ($V_{\mathrm{AC},1} = V_{\mathrm{AC},2}$) at the frequencies $\omega_{\mathrm{e},1}$ and $\omega_{\mathrm{e},2}$ (see eq. (5)). A schematic of the excitation frequencies is shown in Figure 1.

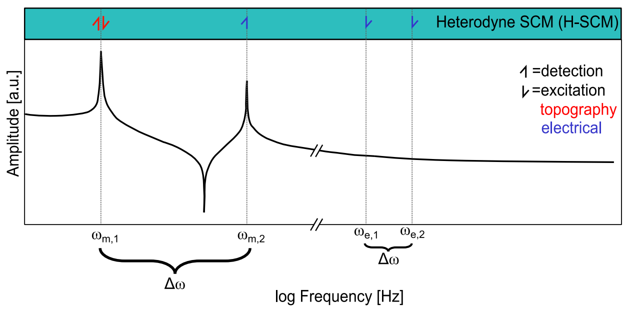

Figure 1: Schematic illustration of the excitation and detection frequencies in H-SCM. The lower part shows the transfer function of the cantilever, where the amplitude is plotted vs the logarithmic angular frequency. The upper part shows the excitation frequencies (↓) and the detection frequencies (↑) of the applied frequencies. The red arrow corresponds to topography- and the blue arrow to the electrical signal. Representation of Fig. 1 was inspired by [18,26]. A comparison of Heterodyne Kelvin Probe Force Microscopy (H-KPFM) and H-SCM can be found in Supporting Information File 1.

The electrical detection frequency (300 - 420 kHz) is several hundred kilohertz away from the frequency of mechanical oscillation (65 - 80 kHz), effectively reducing crosstalk between the topographical and capacitive images.

We select the excitation frequencies to lie at the nth and the $n + 1$th multiple of the frequency gap $\Delta\omega = (\omega_{m,2} - \omega_{m,1})$ (see Figure 1), respectively. We then use lock-in detection to measure the induced mechanical excitation at exactly at the second harmonic of the cantilever ($\omega_{m,2}$).

Single-frequency Electrostatic Force Microscopy to measure the first capacitive gradient C'

To obtain a quantitative comparison of the signal contributions in the signals based on the first and the second capacitance gradient we performed single-frequency excitation EFM (SF-EFM) measurements as comparison to the multi-frequency approach described above. In the fixed-frequency configuration, we use lock-in amplification to detect the second harmonic force component at $2\omega_e$ induced by a single-frequency (ω_E) stimulus (see eq. (3c)).

To enhance the signal we select ω_E such that $2\omega_E$ coincides with the second resonance of the cantilever ($2\omega_E = \omega_{m,1} + \omega_E = \omega_{m,2}$). We relate the numerical value of the capacitance gradient to the detected amplitude via the cantilever's frequency-dependent spring constant $k(\omega)$ by:

$$\frac{\partial C}{\partial z} = C' = \frac{4\, A_{\text{det}} \cdot k(\omega)}{V_{\text{AC}}^2} \tag{9}$$

For the variable-frequency detection of C' we apply two AC voltages of the same magnitude ($V_{AC,1} = V_{AC,2}$) at frequencies n and $(n + 1)$ times the second resonance frequency $\omega_{m,2}$. According to eq. (7a), this will excite an oscillation at $\omega_{m,2}$ with an amplitude proportional to C'.

Silicon micro capacitors

To compare and verify the C' and C'' signal dependency as a function of z during several force-distance curves from the literature with our data we performed experiments on one of the prepared "microcapacitors" you can see in Figure 2.

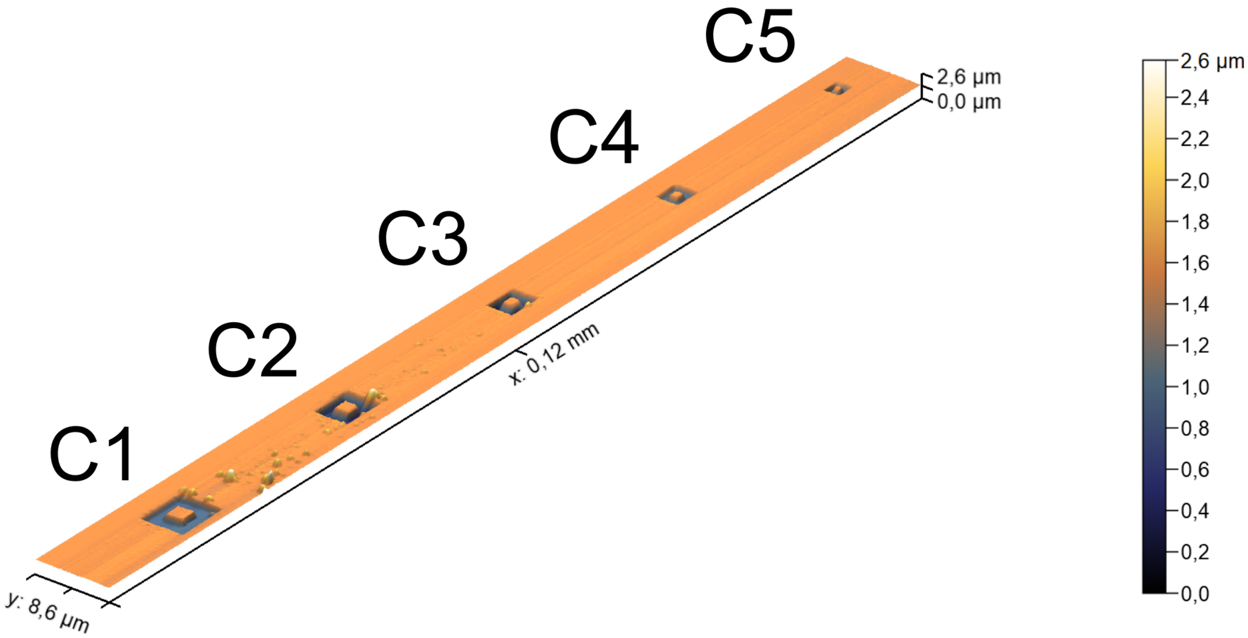

Figure 2: Topography of the five different capacitors C1 to C5 that were produced to have specific capacitors with known capacity. The picture was conducted with the μmasch's HQ:NSC18/Pt Cantilever and analysed with Gwyddion 2.61.

The microcapacitors were produced from scratch by focused ion beam (FIB) milling on a Silicon wafer which was thermally modified so that it has a 300 nm layer of SiO_2 on it. After that the Silicon wafer was placed in the Pt sputter machine and sputtered 14 nm on it. The final substrate had the following layers of Si/300 nmSiO_2 /14 nmPt. A mask was used to mill a trench into the sample until the underlaying Si substrate was visible so that the microcapacitors stick out of surface. This gives a defined nano-structure with known capacitance.

Results and Discussion

To investigate whether the C''-sensitive detection leads to an improved spatial resolution of H-SCM as compared to conventional methods, we calculate the distance-dependence of the first- and second-order capacity gradients in an ideal cantilever. We compare our calculations to experimentally-obtained force-distance curves. We then show the first practical examples of high-frequency capacitive spectra obtained by this method in etched SiO_2 microcapacitors, along with high-resolution high-frequency capacitance-images obtained over self-assembled molecular Perfluoroalkyl-Alkane $F(CF_2)_{14}(CH_2)_{20}H$ (F14H20).

Tip-sample capacitance

The total capacitance between the sample and the cantilever consists of contributions from the tip apex, tip cone, lever and some additional stray capacitance caused by the signal cables in the AFM head (Figure 3). Whereas the apex capacitance contains the desired local information, the stray capacitance from cone, lever and cables produces a background signal that effectively reduces the lateral resolution of the local capacitance measurement. Practically, these signal contributions can be discerned by their respective distance dependence.

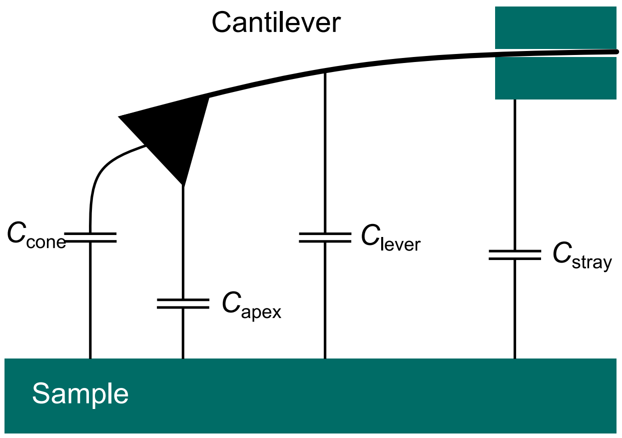

Figure 3: Schematic illustration of tip apex, tip cone, lever and stray capacitance. The contribution of the tip-apex contains the most localized part of the overall capacitance signal. The mesoscopic tip cone and the macroscopic cantilever, on the other hand, contribute to long-ranged stray capacitance, effectively delocalizing the signal.

To further investigate this distance dependence, we compare experimental force-distance spectra to analytical and numeric models from the literature. In particular, we combine the models for the apex contribution of Hudlet et al.[49] with the cone and lever contributions from Colchero et al.[50,51], respectively. The full equations for the force together with the resulting capacitance used here are given in the appendix (see eqs. (12) to (17) and Figure 10).

In Figure 4 (a) and (b), we compare the respective contributions to the first and second capacitance-gradients together with the corresponding electrostatic forces during a typical AFM experiment as

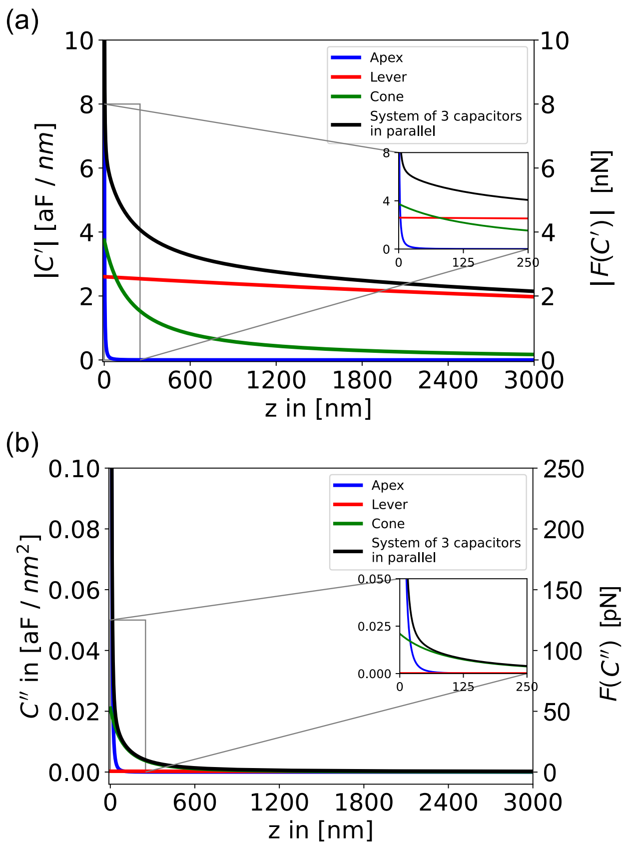

Figure 4: Contributions of the respective components to the (a) first numeric derivative C' and (b) second numeric derivative C'' of the capacitance versus z distance between tip and sample. Additionally, the respective force (a) $F(C')$ and (b) $F(C'')$ was plotted as well against z. The NuNano SPARK 70 Pt cantilever ($w = 30\,\mu\text{m}$, $l = 225\,\mu\text{m}$, $\alpha = 11\,\text{deg}$, $h = 12\,\mu\text{m}$, $\theta = 25\,\text{deg}$, $r = 18\,\text{nm}$, $\delta = 3.7 \cdot 10^{-7}$) was used for the calculations with an mechanical amplitude of $A_\text{m} = 10\,\text{nm}$, an excitation voltage of $V_\text{AC} = 2\,\text{V}$, and a total amount of calculated points of 100,000. The blue line marks the apex, the green line the cone, the red line the lever and the black line marks the entire system of the three components in parallel.

a function of tip-sample distance z. For the force calculations, we used eq. (8) together with the parameters of a regular EFM cantilever (NuNano SPARK 70 Pt) and an electrical drive of $V = 2\,\text{V}$ and a mechanical amplitude of $A_\text{m} = 10\,\text{nm}$. Comparing the graphs, we can immediately see that the total C' signal retains a significant long-range contribution even at a tip-sample separation of 3000 nm (Figure 4 (a)). In contrast, the C'' signal shown in drops more rapidly over a short distance z (Figure 4 (b)), indicating a reduced influence of long-ranged contributions to the force signals.

A measure of how much the signal is disturbed by non-local long-ranged contributions is the ratio between the apex contribution to the total signal at a given distance z. At a typical tip-sample separation of 10 nm, the apex signal makes up more than 82 % of the complete C'' signal while the apex contribution on the first capacitance gradient only makes up less than 10 % of the total C' signal. In closer proximity of 1 nm distance to the sample, the apex contribution in the C'' signal increases to 99.8 %, whereas the C' signal still contains a significant amount of non-local signal contributions with 62 % apex vs. 38 % cone and lever signal. Another way to quantify the "locality" a force signal is to investigate the tip sample separation, where the tip apex contribution surpasses the lever plus cone contributions within Figure 4. This is true in Figure 4(a) for distances smaller than ≈ 3 nm while in Figure 4 (b) this is the case even for distances smaller than ≈ 20 nm. Comparing the absolute values of the forces, however, we see that H-SCM yields much weaker forces: At a tip-sample distance of 10 nm, the AM-based operation leads to a force of $F_{ES}(C') = 6.7$ nN, as compared to $F_{ES}(C'') = 280$ pN for H-SCM. So the resulting electrostatic force and thereby the expected force is more than a factor of 24 lower for H-SCM. So the improved lateral resolution comes at the price of a reduced signal-to-noise ratio (SNR).

To reproduce these findings experimentally, we performed force-distance spectroscopy on the etched microcapacitors (Figure 2 in the Methods and Experimental section). The resulting curves of the C' and C'' signal qualitatively reproduced the simulation results (Figure 5): Whereas the C'' signal only emerged from the noise at distances of less than 500 nm, the C' signal shows a monotonic decrease over the full 3 µm of vertical travel. Compared to the simulations, the experimental C' signal shows a slower decrease, indicating a stronger influence by the tip cone. The direct comparison of the model and the data of the second and first capacity gradient can be found in Supporting Information Files 15 and 16, respectively. These results clearly show that the H-SCM method produced an electrostatic force signal that is highly local with suppressed stray contributions from cone and lever.

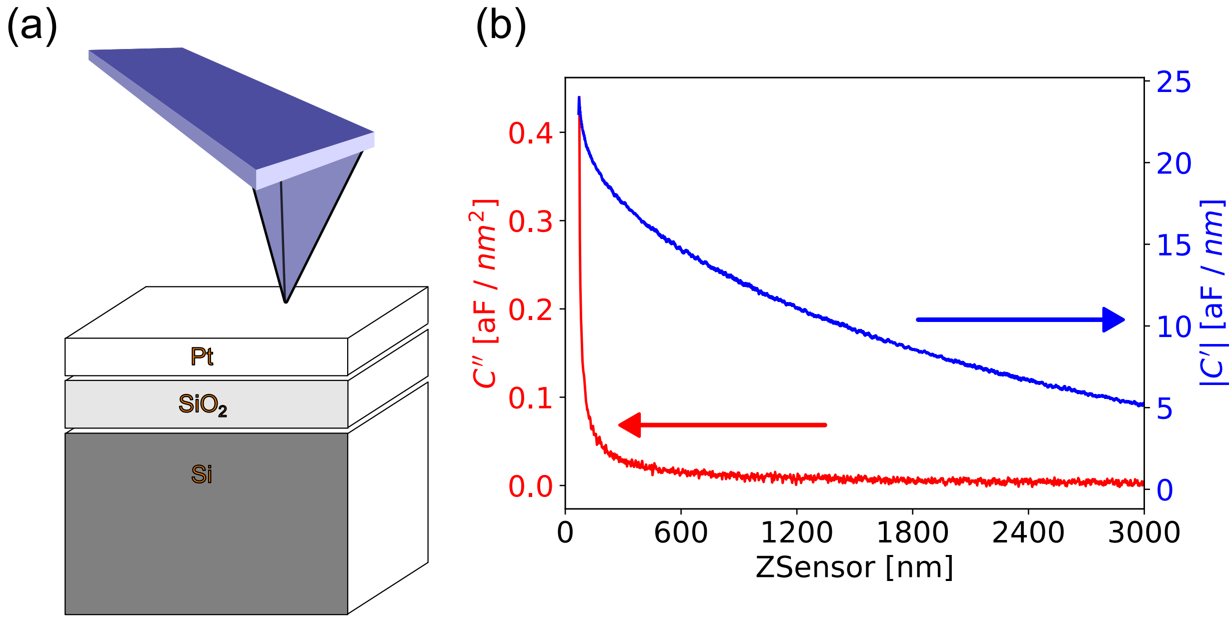

Figure 5: Comparison of the C'' and the C' single force curves (b) of a microcapacitor (a) while doing H-SCM (see eqs. (7b) and (8)) and compared with the detection of 2ω (see eqs. (3c) and (9)). This was conducted with the NuNano's SPARK 70 Pt cantilever.

Dielectric spectroscopy

The advantage of the multi-frequency excitation approach of H-SCM is that we can choose arbitrary frequencies for the electrostatic excitation. As the tip-sample capacitance is influenced by the dielectric properties of the material in the tip-sample gap, the frequency-dependent electrostatic force represents the local dielectric function. To demonstrate the feasibility of dielectric nano-spectroscopy, we performed H-SCM frequency-spectroscopy in three different locations on the microcapacitor sample where we expect a vastly different dielectric response. A first spectrum was recorded on one of the microcapacitors ($C3$, see methods). Then, we measured on the bare Si where we expect a fresh native oxide layer of $\approx$5 nm thickness (Si). Lastly, we measured on a particle of unknown origin (Dirt, visible in Figure 2). The frequency sweeps were performed by keeping the tip position and amplitude fixed, varying the two heterodyne excitation frequencies while keeping their separation fixed, and recording the resulting excitation amplitude at the second mechanical resonance. All spectra were normalized against a reference spectrum recorded on the bare substrate far away from the capacitors to compensate any frequency-response arising from the stray capacitance in the signal paths and cantilever.

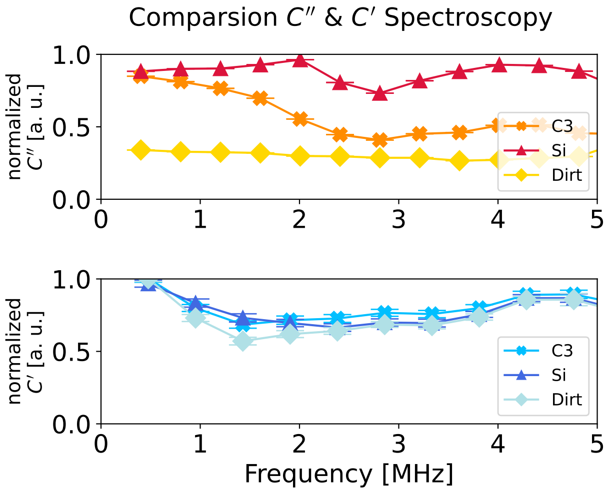

Figure 6: Comparison of the normalized C'' (red colors on top) and normalized C' (blue colors at the bottom) frequency sweep on one of the the capacitors (C3) (cross symbols), the milled Silicon (Si) (triangle symbols), and a measurement on a particle of unknown origin (Dirt) (square symbols). This experiment was conducted with the μmasch's HQ:NSC18/Pt Cantilever. The non-normalized data can be seen in Supporting Information Files 2 to 5 and 8 to 11.

The electrostatic signal of the capacitor C3 showed a drop at around 2 MHz in Figure 6. When considering the capacitance of C3 of (183 ± 1) aF and the drop-off frequency ω_d of the capacitance at 1.7 MHz, we can calculate the resistance R via the RC time ($R \cdot C = 1/\omega_d$) as $R \approx 3200\,\mathrm{M\Omega}$. This value is close to the value of 8 GΩ, taking into account the electrical resistivity of silicon of $\rho_{\mathrm{Si}} = 2.3 \cdot 10^{12}\,\mathrm{n\Omega\,m}$ and a thickness of the SiO_2 of 300 nm.

The C'' signal of the bare Si was stable over the whole range of excitation frequencies and only dropped at a much higher frequency around 24 MHz (see Supporting Information File 4). In the frequency response of the undefined particle, we found little to no signal response, even at low excitation frequency. A rise of the signal at around 6 MHz could be observed in all the C'' signals at that frequency (see Supporting Information File 2) which we attribute to a capacitive singularity in the electrical connection to the sample. We observed a similar behavior in the frequency range between 5 and 10 MHz and around 17 MHz. We want to point out that we used standard AFM equipment with no special means to control the impedance of the electrical connections. To obtain more trustworthy data in the frequency range above 5 MHz will require specialized sample- and cantilever holders with coaxial electric connections.

To compare these results with the conventional AM-based SCM approach, we repeated the spectroscopy experiments for the C' signal based on the second term in eq. (7a) (Figure 6, non-normalized data in Supporting Information Files 8 to 10). In comparison to the H-SCM data, the C' frequency sweep looked very similar on the different structures. We think that this reduction in contrast is caused by the stronger influence of long-ranged interactions in the C' signal, reducing the overall impact of the local interaction of the tip apex with the area of interest.

Imaging C′ versus C″

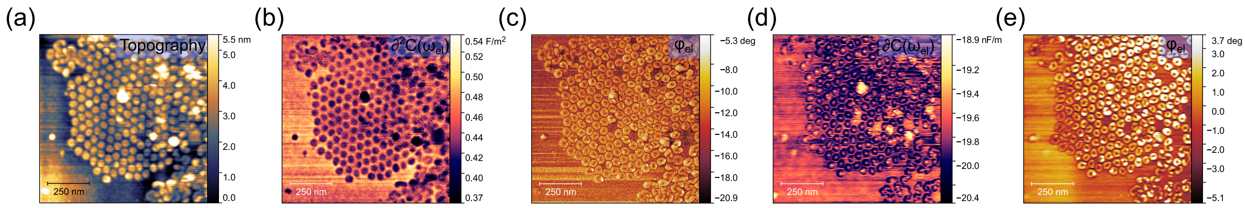

Figure 7: H-SCM images taken on F14H20 with (a) the topography, (b) the C'' picture at 1.59 and 1.98 MHz, (c) electric phase φ_{el} of the C'' signal at 1.59 and 1.98 MHz, (d) the C' picture at 235.579 kHz, (e) electric phase φ_{el} of the C' signal at 235.579 kHz. The full picture can be found in Supporting Information File 14. This was conducted with the μmasch's HQ:NSC18/Pt Cantilever.

To demonstrate the capabilities of H-SCM as an imaging method, we performed experiments on self-assembled nanostructures consisting of the amphiphilic molecule Perfluoroalkyl-Alkane $F(CF_2)_{14}(CH_2)_{20}H$ (F14H20) (Figure 7). On the silicon substrate, the F14H20 formed groups of spherical particles with a diameter of (40 ± 5) nm (Figure 7(a))[52,53]. Simultaneously with the topography, we recorded the C'' amplitude and phase at an electrical excitation frequency of 1.59 and 1.98 MHz. In Figure 7(b) we see a sharp contrast between the F14H20 aggregates and the silicon substrate. Interestingly, the image of the C' signal measured at 236 kHz showed a different contrast. In particular, both the amplitude and phase contrast of the particles changes from left to right, indicating long ranged background signal.

Conclusion

In this paper, we have presented a novel method for high-resolution nanoscale capacitance characterization based on multi-frequency electrostatics. The key advantage of the multi-frequency approach of H-SCM is that it allows for operation at almost arbitrary frequencies, enabling the measurement of the local dielectric function over a wide range of frequencies. In comparison to existing SCM operation modes, H-SCM leads to a significant reduction of signal background, which results in higher locality of the measurements with less cross-talk. This is due to the fact that the second capacitance gradient is less affected by long-range interactions, such as those from the tip cone and lever. We demonstrate the reliable operation using standard AFM equipment together with an external LIA up to a frequency of 5 MHz. At higher frequencies (up to 50 MHz in our case), the signals were dominated by impedance effects from the signal connections. Thus, to move towards reliable measurements at higher frequencies, specialized HF-equipment with coaxial signal connections will be required.

Our analytical simulations of the distance-dependent tip-sample capacitance showed that current models are not able to fully simulate the experimental data. Thus, to enable quantitative measurements of the tip-sample capacitance, further measures such as improved tip-sample models or full numerical simulations will be required. This will pave the way for quantitative studies of dielectric effects in nanoscale systems in materials science, biology, and nanotechnology.

Experimental (optional)

Polymer blend samples

We used the Perfluoroalkyl-Alkane $F(CF_2)_{14}(CH_2)_{20}H$ (F14H20) samples that we bought from SPM Labs LLC.

Microcapacitors

The Si wafers "CZ" were bought from "Si-Mat" with a diameter of 150 mm, a surface orientation <100>, a thickness of (675 ± 20) µm, a resistivity of 1.5 - 4.0 Ω cm, and with a p-type doping with B-atoms. These wafers were thermally oxidised with 300 nm SiO_2. To sputter Pt on top of the silicon wafer the Pt sputter machine Compact Coating Unit (CCU) 010/LV with the sputter head SP010 was used to sputter 14 nm on top of the wafer. The microcapacitors were then milled out of the surface by a FIB from FEI Nova600 Nanolab with a dual-beam Ga^+ ion beam.

Heterodyne Scanning Capacitance Microscopy (H-SCM) Measurements

H-SCM was measured on an Oxford Instruments/Asylum Research MFP-3D Infinity AFM in a nitrogen glovebox (level of humidity below 0.3 %, level of oxygen below 0.1 %) for all experiments. The typical resonance frequency of the Pt/Ir coated conductive cantilevers (NuNano model: SPARK-150Pt; μmasch model: HQ:NSC18/Pt) was ≈ 75 kHz, spring constant of 2 to 3 $\frac{\mathrm{N}}{\mathrm{m}}$, a tip radius of 18 nm and a tip height of 10 to 18 µm. The topography feedback was performed with amplitude modulation (AM) on the first eigenmode $\omega_{\mathrm{m},1}$ and the oscillation amplitude was kept to approximately ≈ 70 - 90 nm for all measurements. The force spectroscopy measurements were done with a z-Rate of 0.2 Hz and a force distance of 8 µm for all samples.

We used a Zurich Instruments HF2 lock-in amplifier for all experiments including to perform the H-SCM measurements. The electric drive amplitude of the $V_{\mathrm{AC},1} = V_{\mathrm{AC},2}$ signal varied between 3 and 5 V depending on the obtained signal from the sample. We grounded the sample via the sample holder with an external wire to ground level of the Zürich Lock-In Amplifier. The applied V_{AC} was applied to the tip directly while the AFM head connections were switched off. The setup of the AFM is shown in Figure 8. The electrical connection from the LIA to the cantilever with the two excitation voltages was realized by using a direct cable connection. The sample was always grounded to the ground level of the LIA. A scheme can be seen in Figure 8.

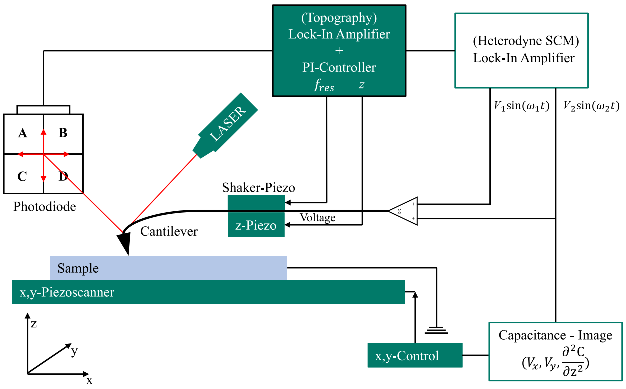

Figure 8: Schematic setup of H-SCM. Additionally to a regular AFM, two different voltages are applied to the cantilever with different frequencies respectively.

Focused ion beam (FIB)

FIB of the cantilever was conducted using a LEO Gemini instrument from Zeiss. It was used with an acceleration voltage of 3 kV.

Appendix

Equations to calculate the C'' and C' Signal from the voltages

Equation (10) shows the detailed expression shown in eq. (8). Within the detected amplitude from the LIA A_{det} is the Voltage from the LIA ($V_{\text{H-SCM}}$) and the amplification factor $\Xi_{\text{amp,d2C}}$ of this voltage from the LIA in H-SCM mode. The frequency dependent spring constant $k(\omega)$ in eq. (8) contains the inverse optical lever sensitivity (InvOLS) of the second harmonic ($InvOLS_2$) and the spring constant of the second resonance (k_2) shown in eq. (10). It is important to note that the InvOLS and the spring constant on the seconds resonance is not the same as measured on the first resonance by the method of Sader et al.[54]. It is rather necessary to calculate the properties of the cantilever for the respective eigenmodes[55].

$$\frac{\partial^2 C}{\partial z^2}(\omega) = C''(\omega) = \frac{16 \cdot V_{\text{H-SCM}}(\omega) \cdot InvOLS_2(\omega) \cdot k_2(\omega)}{A_{\text{m}} \cdot V_{\text{AC}}^2 \cdot \Xi_{\text{amp,d2C}}} \tag{10}$$

Equation (11) shows the detailed expression shown in eq. (9). In the expression A_{det} is the detected voltage from the LIA ($V_{\text{SF-EFM}}$) and again an amplification factor $\Xi_{\mathrm{amp,dC}}$ of the signal captured with the LIA with the SF-EFM mode. The frequency-dependent spring constant $k(\omega)$ is the same as above and consists of $InvOLS_2$ and k_2.

$$\frac{\partial C}{\partial z}(\omega) = C'(\omega) = \frac{4 \cdot V_{\text{SF-EFM}}(\omega) \cdot InvOLS_2(\omega) \cdot k_2(\omega)}{V_{\mathrm{AC}}^2 \cdot \Xi_{\mathrm{amp,dC}}} \tag{11}$$

Full double excitation force equations

Full overview of the electric amplitude contributions at various frequencies while activating the heterodyne Scanning Capacitance Microscopy (H-SCM) mode. For simplicity, we will use the following substitutions $\omega_{\mathrm{m}}^1 t = O$, $\omega_{\mathrm{e}} t = E$, $\omega_{\mathrm{mod}} t = M$, $V_{\mathrm{CPD}} - V_{\mathrm{DC}} = \Delta$, $\hat{V}_{\mathrm{AC}} = V$, and $A_m^1 = A$ In Table 1 is the overview of the force components at various frequencies for the resulting static, ω and 2ω force components acting on the cantilever.

Table 1: Overview of the components of the multi-frequency electrostatic force microscopy.

Frequency	**Amplitude**
DC	$1/2C'[\Delta^2 + U^2/4]$
$2M$	$1/8C'U^2$
O	$1/2C''A[\Delta^2 + U^2/4]$
$O \pm 2M$	$1/16C''AU^2$
$E \pm M$	$1/2C'U\,\Delta$
$O \pm (E \pm M)$	$1/4C''AU\Delta$
$2E$	$1/8C'U^2$
$2(M \pm E)$	$1/16C'U^2$
$O \pm 2E$	$1/16C''AU^2$
$O \pm 2(E \pm M)$	$1/32C''AU^2$

Tip-sample capacity model

We used the model of Hudlet et al.[49] for the tip apex and in addition used the sum of cone and lever distribution of Colchero et al.[50,51]. The cantilever can be modeled as a tilted plate capacitor with a truncated cone at the end of the cantilever and with a sharp round tip apex at the end of the tip cone. This is shown schematically in Figure 9.

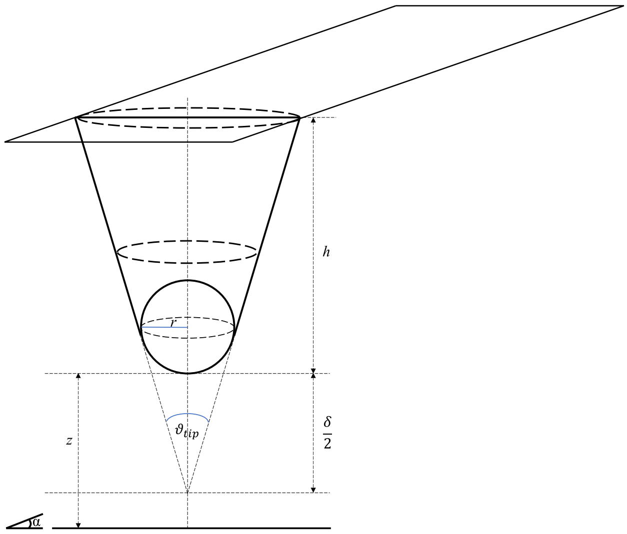

Figure 9: Auxiliary sketch of the capacitance model of the truncated cone with spherical apex. Here h is the height of the tip, r is the radius of the sphere, ϑ_{tip} is the opening angle of the tip, δ is the truncated part of the cone and z is the distance between sample and tip apex in respect to the surface normal of the sample. α is the angle between the surface and the lever of the cantilever.

In this case the electrostatic force for the lever is given by eq. (12).

$$F_{\mathrm{lever}}(z) = \frac{2\tan^2(\frac{\alpha}{2})}{\alpha^2}\,\varepsilon_0\,V^2_{\text{tip-sample}}\,\frac{l\,w}{h^2}\,\frac{1}{\left[\left(1+\frac{z}{h}\right)\cdot\left(1+\frac{z+2l\tan\left(\frac{\alpha}{2}\right)}{h}\right)\right]}\text{[50,51]}. \tag{12}$$

Integration due to eq. (1) yields

$$\begin{gathered}C_{\mathrm{lever}}(z) = \frac{2\tan^2(\frac{\alpha}{2})}{\alpha^2}\,\varepsilon_0\,V^2_{\text{tip-sample}}\,\frac{l\,w}{h^2}\\ \cdot\frac{h^2\cot\left(\frac{\alpha}{2}\right)\left(\ln(h+z)-\ln\left(\cos\left(\frac{\alpha}{2}\right)(h+z)+2l\sin\left(\frac{\alpha}{2}\right)\right)\right)}{2l},\end{gathered} \tag{13}$$

where ε_0 is the dielectric constant of the vacuum. The dimensions of the lever are given by its width w, its length l and the height of the tip cone h. The lever is tilted by the angle $\alpha = \vartheta_{\mathrm{lever}}$. The tip cone can be approximated by a truncated cone (Figure 9). The electrostatic force as a function of distance between tip cone and sample is given by eq. (14).

$$F_{\text{cone}}(z) = \frac{4\,\pi}{(\pi - \vartheta_{\text{tip}})^2}\,\varepsilon_0\,V^2_{\text{tip-sample}} \cdot \left[\ln\left(\frac{z - \frac{\delta}{2} + h}{z + \frac{\delta}{2}}\right) - \sin\left(\frac{\vartheta_{\text{tip}}}{2}\right)\frac{h - \delta}{z - \frac{\delta}{2} + h}\cdot\frac{z - \frac{\delta}{2}}{z + \frac{\delta}{2}}\right] [50,51] \tag{14}$$

with the open angle of the tip cone (ϑ_{tip}), and the height of the truncated part of the cone ($\delta = r/\tan^2(\vartheta_{\text{tip}}/2)$)[50,51]. Integration of this equation to obtain the capacitance yields

$$C_{\text{cone}}(z) = 2\frac{4\pi\varepsilon_0}{(\vartheta_{tip} - \pi)^2}\left[\sin\left(\frac{\vartheta_{tip}}{2}\right)(h\ln(2f_1) - \delta\ln(f_2)) + f_1\ln\left(\frac{f_2}{2f_1}\right) + (\delta - h)\ln(f_2)\right], \tag{15}$$

where $f_1 = z - \frac{\delta}{2} + h$ and $f_2 = 2z + \delta$.

The tip apex is approximated as a sphere over an infinite surface (Figure 9). The corresponding electrostatic force between a tip apex and the surface is given in eq. (16).

$$F_{\text{apex}}(z) = \pi\,\varepsilon_0\,r^2\,V^2_{\text{tip-sample}}\left[\frac{1 - \sin\left(\frac{\vartheta_{\text{tip}}}{2}\right)}{z\left(z + r\left(1 - \sin\left(\frac{\vartheta_{\text{tip}}}{2}\right)\right)\right)}\right][49]. \tag{16}$$

Hence, the capacitance is given by

$$C_{\text{apex}}(z) = 2\pi\varepsilon_0\,r\ln\left(\frac{z + r\left(1 - \sin\left(\frac{\vartheta_{\text{tip}}}{2}\right)\right)}{z}\right). \tag{17}$$

When you plot the capacity of the cantilever against the distance between the tip and the sample z you get Figure 10. The parameter were taken from the Website of the producer of the NuNano SPARK 70 Pt cantilever: $w = 30\,\mu\text{m}$, $l = 225\,\mu\text{m}$, $\alpha = 11\,\text{deg}$, $h = 12\,\mu\text{m}$, $\vartheta_{\text{cone}} = 25\,\text{deg}$, $r = 18\,\text{nm}$, and $V_{\text{AC}} = 2\,\text{V}$.

In order to get the first C' and second capacity gradient C'' of the relevant parts of the cantilever,

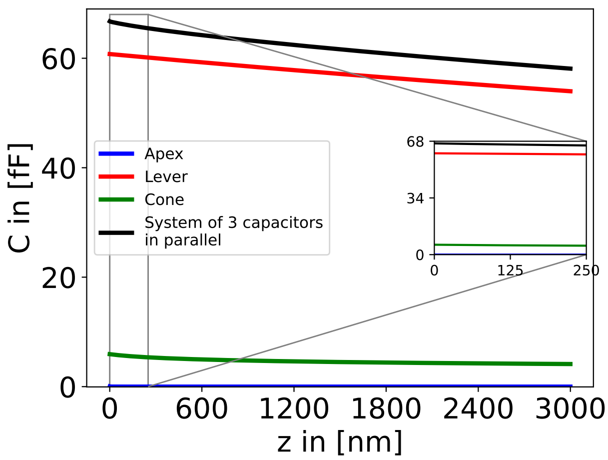

Figure 10: Contributions of the respective components to the numeric capacity C versus z distance between tip and sample. The properties of the NuNano SPARK 70 Pt cantilever ($w = 30\,\mu\text{m}$, $l = 225\,\mu\text{m}$, $\alpha = 11\,\text{deg}$, $h = 12\,\mu\text{m}$, $\theta = 25\,\text{deg}$, $r = 18\,\text{nm}$, $\delta = 3.7 \cdot 10^{-7}$) with an mechanical amplitude of $A_\text{m} = 10\,\text{nm}$, an excitation voltage of $V_\text{AC} = 2\,\text{V}$, and a total amount of calculated points of 100,000, was used for the calculations. The blue line marks the apex, the green line the cone, the red line the lever and the black line marks the entire system of the three components in parallel.

we used the onward and backward differentiation seen in eq. (18) and the central differential quotient of the second order seen in eq. (19) is used, respectively.

$$f'(x) = \frac{f(x+h) - f(x-h)}{2h} \tag{18}$$

The step size was chosen to be $1 \cdot 10^{-10}\,\text{m}$ with a total amount of $1,000,000$ steps.

$$f''(x) = \frac{f(x+h) - 2f(x) + f(x-h)}{h^2} \tag{19}$$

Again, the step size of this was chosen to be the same as for the first derivative.

The model of the first and second capacity gradient can be found in Figure 4 (a) and (b), respectively.

Supporting Information

Supporting information features a comparison of the working principles of H-KPFM and H-SCM, all the raw and normalized data of the H-SCM frequency spectroscopy, the full comparison of the H-SCM, SF-EFM, and H-KPFM images on the F14H20 structures, and finally a comparison of the model data and the measured data on the microcapacitors.

Supporting Information File 1:

File Name: H-KPFM_and_H-SCM_scheme_working_principle_two.pdf

File Format: PDF

Title: Schematic comparison of the excitation and detection frequencies in H-KPFM and H-SCM. The lower part shows the transfer function of the cantilever, where the amplitude is plotted vs the logarithmic angular frequency. The upper part shows the excitation frequencies (↓) and the detection frequencies (↑) of the applied frequencies. The red arrow corresponds to topography- and the blue arrow to the electrical signal[18,26,56].

Supporting Information File 2:

File Name: Freq_Sweep_Comparison_d2C_vs_Frequency.pdf

File Format: PDF

Title: Non-normalized data of the comparison of the C'' frequency sweep shown in Figure 6 on the four spots while in H-SCM (see eq. (8)). This was conducted with the μmasch's HQ:NSC18/Pt cantilever.

Supporting Information File 3:

File Name: Freq_Sweep_Comparison_d2C_vs_Frequency_zoom.pdf

File Format: PDF

Title: Zoom of the non-normalized data from the comparison of the C'' frequency sweep shown in Figure 6 on the four spots while in H-SCM (see eq. (8)). This was conducted with the μmasch's HQ:NSC18/Pt cantilever.

Supporting Information File 4:

File Name: Freq_Sweep_Comparison_d2C_vs_Frequency_normed.pdf

File Format: PDF

Title: Normalized data of the C'' frequency sweep shown in Figure 6 on the three spots while in H-SCM (see eq. (8)). This was conducted with the μmasch's HQ:NSC18/Pt cantilever.

Supporting Information File 5:

File Name: Freq_Sweep_Comparison_d2C_vs_Frequency_normed_zoom.pdf

File Format: PDF

Title: Zoomed and normalized data of the C'' frequency sweep shown in Figure 6 on the three spots while in H-SCM (see eq. (8)). This was conducted with the μmasch's HQ:NSC18/Pt cantilever.

Supporting Information File 6:

File Name: Freq_Sweep_Comparison_elec_Phase_d2C_vs_Frequency.pdf

File Format: PDF

Title: Non-normalized data of the phase signal φ spectra of the comparison from the C'' frequency sweep shown in Figure 6 on the four spots while in H-SCM (see eq. (8)). This was conducted with the μmasch's HQ:NSC18/Pt cantilever.

Supporting Information File 7:

File Name: Freq_Sweep_Comparison_elec_Phase_d2C_vs_Frequency_zoom.pdf

File Format: PDF

Title: Zoom of the non-normalized data of the phase signal φ spectra of the comparison from the C'' frequency sweep shown in Figure 6 on the four spots while in H-SCM (see eq. (8)). This was conducted with the μmasch's HQ:NSC18/Pt cantilever.

Supporting Information File 8:

File Name: Freq_Sweep_Comparison_dC_vs_Frequency.pdf

File Format: PDF

Title: Non-normalized data of the comparison of the C' frequency sweep shown in Figure 6 on the four spots while in SF-EFM mode (see eq. (9)). This was conducted with the μmasch's HQ:NSC18/Pt cantilever.

Supporting Information File 9:

File Name: Freq_Sweep_Comparison_dC_vs_Frequency_zoom.pdf

File Format: PDF

Title: Zoom of the non-normalized data of the comparison of the C' frequency sweep shown in Figure 6 on the four spots while in SF-EFM mode (see eq. (9)). This was conducted with the μmasch's HQ:NSC18/Pt cantilever.

Supporting Information File 10:

File Name: Freq_Sweep_Comparison_dC_vs_Frequency_normed.pdf

File Format: PDF

Title: Normalized data of the C' frequency sweep shown in Figure 6 on the three spots while in SF-EFM mode (see eq. (9)). This was conducted with the μmasch's HQ:NSC18/Pt cantilever.

Supporting Information File 11:

File Name: Freq_Sweep_Comparison_dC_vs_Frequency_normed_zoom.pdf

File Format: PDF

Title: Zoomed and normalized data of the C' frequency sweep shown in Figure 6 on the three spots while in SF-EFM mode (see eq. (9)). This was conducted with the μmasch's HQ:NSC18/Pt cantilever.

Supporting Information File 12:

File Name: Freq_Sweep_Comparison_elec_Phase_dC_vs_Frequency.pdf

File Format: PDF

Title: Non-normalized data of the phase signal φ spectra of the comparison of the C' frequency sweep shown in Figure 6 on the four spots while in SF-EFM mode (see eq. (9)). This was conducted with the μmasch's HQ:NSC18/Pt cantilever.

Supporting Information File 13:

File Name: Freq_Sweep_Comparison_elec_Phase_dC_vs_Frequency_zoom.pdf

File Format: PDF

Title: Zoom of the non-normalized data of the phase signal φ spectra of the comparison of the C' frequency sweep shown in Figure 6 on the four spots while in SF-EFM mode (see eq. (9)). This was conducted with the μmasch's HQ:NSC18/Pt cantilever.

Supporting Information File 14:

File Name: Zeichnung_F14H20_Comparison_dC_d2C_SI.pdf

File Format: PDF

Title: Full version of the H-SCM pictures given in Figure 7. H-SCM pictures made on F14H20 with (a) the topography, (b) the C'' picture at 1.59 and 1.98 MHz, (c) electric phase φ_{el} of the C'' signal at 1.59 and 1.98 MHz, (d) the C' picture at 235.579 kHz, (e) electric phase φ_{el} of the C' signal at 235.579 kHz, (f) the CPD picture, (g) the C'' picture at 15.88 and 16.28 MHz, (h) electric phase φ_{el} of the C'' signal at 15.88 and 16.28 MHz, (i) the picture of the mechanical amplitude at the resonance frequency of 74.580 kHz, and (j) the picture of the mechanical phase at the resonance frequency of 74.580 kHz. This was conducted with the μmasch's HQ:NSC18/Pt Cantilever.

Supporting Information File 15:

File Name: Comparison_Model_&_Data_d2C_vs_ZSensor_data_model_2_500.pdf

File Format: PDF

Title: A comparison of the measured C'' values on various capacitors, as shown in Figure 2, is presented. The measurements, performed using the NuNano SPARK 70 Pt cantilever (solid lines), are contrasted with the theoretical contributions of the respective components to the first numerical derivative C' of the capacitance (dotted lines) as a function of the tip-to-sample distance, z. For the theoretical calculations, the properties of the NuNano SPARK 70 Pt cantilever ($w = 30\,\mu\mathrm{m}$, $l = 225\,\mu\mathrm{m}$, $\alpha = 11\,\mathrm{deg}$, $h = 12\,\mu\mathrm{m}$, $\theta = 25\,\mathrm{deg}$, $r = 18\,\mathrm{nm}$, $\delta = 3.7 \cdot 10^{-7}$) with an mechanical amplitude of $A_{\mathrm{m}} = 10\,\mathrm{nm}$, an excitation voltage of $V_{\mathrm{AC}} = 2\,\mathrm{V}$, and a total amount of calculated points of 100,000, was used for these.

Supporting Information File 16:

File Name: Comparison_Model_&_Data_dC_vs_ZSensor_data_model_2_500.pdf

File Format: PDF

Title: A comparison of the measured C' values on various capacitors, as shown in Figure 2, is presented. The measurements, performed using the NuNano SPARK 70 Pt cantilever (solid lines), are contrasted with the theoretical contributions of the respective components to the first numerical derivative C' of the capacitance (dotted lines) as a function of the tip-to-sample distance, z. For the theoretical calculations, the properties of the NuNano SPARK 70 Pt cantilever ($w = 30\,\mu\text{m}$, $l = 225\,\mu\text{m}$, $\alpha = 11\,\text{deg}$, $h = 12\,\mu\text{m}$, $\theta = 25\,\text{deg}$, $r = 18\,\text{nm}$, $\delta = 3.7 \cdot 10^{-7}$) with an mechanical amplitude of $A_\text{m} = 10\,\text{nm}$, an excitation voltage of $V_\text{AC} = 2\,\text{V}$, and a total amount of calculated points of 100,000, was used for these.

Acknowledgements

This work is based on the preliminary results previously reported in the Bachelor Thesis in Physics named “Tip-sample capacitance in electrostatic force microscopy” by Peter Gregor Reichel (2021, Johannes Gutenberg-Universität Mainz). We acknowledge Dr. Pravash Bista giving helpful ideas in the process of the research. Also, we acknowledge Maren Müller, our technician, for the help to prepare the capacitors.

References

1. Elayarani, P.; Sumathi, T.; Sivakumar, G.; Pragadeswaran, S.; Suthakaran, S.; Sathiyamurthy, S.; Seshadhri, J.; Ayyar, M.; Arularasu, M. V. *Zeitschrift für Phys. Chemie* **2024**, *238* (6), 1–24. doi:10.1515/zpch-2023-0531.

2. Majid, F.; Bashir, M.; Bibi, I.; Ayub, M.; Khan, B. S.; Somaily, H. H.; Al-Mijalli, S. H.; Nazir, A.; Iqbal, S.; Iqbal, M. *Zeitschrift für Phys. Chemie* **2023**, *237* (9), 1345–1360. doi:10.1515/zpch-2022-0097.

3. Iqbal, Z.; Imran, M.; Latif, S.; Nazir, A.; Ibrahim, S. M.; Ahmad, I.; Iqbal, M.; Iqbal, S. *Zeitschrift für Phys. Chemie* **2023**, *237* (8), 1139–1152. doi:10.1515/zpch-2022-0113.

4. Ali, F.; Safdar, A.; Younas, U.; Sillanpaa, M.; Pervaiz, M.; Nazir, A.; Naeem, M.; Iqbal, M.; Al-Kahtani, A. A.; Tighezza, A. M. *Zeitschrift für Phys. Chemie* **2023**, *237* (4-5), 599–616. doi:10.1515/zpch-2022-0098.

5. Nazir, A.; Alam, S.; Alwadai, N.; Abbas, M.; Bibi, I.; Ali, A.; Ahmad, N.; Al Huwayz, M.; Iqbal, M. *Zeitschrift für Phys. Chemie* **2023**, *237* (11), 1733–1751. doi:10.1515/zpch-2023-0331.

6. Arif, H.; Yasir, M.; Ali, F.; Nazir, A.; Ali, A.; Al Huwayz, M.; Alwadai, N.; Iqbal, M. *Zeitschrift für Phys. Chemie* **2023**, *237* (6), 689–705. doi:10.1515/zpch-2023-0224.

7. Sahoo, K. K.; Pradhan, D.; Ghosh, S. P.; Gartia, A.; Kar, J. P. *Phys. Scr.* **2024**, *99* (2), 025934. doi:10.1088/1402-4896/ad196b.

8. Zhu, C.; Liu, A.; Liu, G.; Jiang, G.; Meng, Y.; Fortunato, E.; Martins, R.; Shan, F. *J. Mater. Chem. C* **2016**, *4* (45), 10715–10721. doi:10.1039/C6TC02607A.

9. Paily, R.; DasGupta, A.; DasGupta, N.; Bhattacharya, P.; Misra, P.; Ganguli, T.; Kukreja, L. M.; Balamurugan, A.; Rajagopalan, S.; Tyagi, A. *Appl. Surf. Sci.* **2002**, *187* (3-4), 297–304. doi:10.1016/S0169-4332(01)01040-6.

10. Robertson, J. *Reports Prog. Phys.* **2006**, *69* (2), 327–396. doi:10.1088/0034-4885/69/2/R02.

11. Werner, F.; Babbe, F.; Elanzeery, H.; Siebentritt, S. *Prog. Photovoltaics Res. Appl.* **2019**, *27* (11), 1045–1058. doi:10.1002/pip.3196.

12. *Impedance Spectroscopy*; Barsoukov, E., Macdonald, J. R., Eds.; Wiley, 2005; doi:10.1002/0471716243.

13. Shi, N.; Ramprasad, R. *J. Comput. Mater. Des.* **2007**, *14* (1), 133–139. doi:10.1007/s10820-006-9034-9.

14. Pang, H.-S.; Xu, H.; Tang, C.; Meng, L.-K.; Ding, Y.; Xiao, J.; Liu, R.-L.; Pang, Z.-Q.; Huang, W. *Org. Electron.* **2019**, *65* (September 2018), 275–299. doi:10.1016/j.orgel.2018.09.025.

15. Yalcinkaya, Y.; Rohrbeck, P. N.; Schütz, E. R.; Fakharuddin, A.; Schmidt-Mende, L.; Weber, S. A. *Adv. Opt. Mater.* **2024**, *12* (8), 1–12. doi:10.1002/adom.202301318.

16. Binnig, G.; Rohrer, H.; Gerber, C.; Weibel, E. *Phys. Rev. Lett.* **1982**, *49* (1), 57–61. doi:10.1103/PhysRevLett.49.57.

17. Binnig, G.; Quate, C. F.; Gerber, C. *Phys. Rev. Lett.* **1986**, *56* (9), 930–933. doi:10.1103/PhysRevLett.56.930.

18. Axt, A.; Hermes, I. M.; Bergmann, V. W.; Tausendpfund, N.; Weber, S. A. L. *Beilstein J. Nanotechnol.* **2018**, *9* (1), 1809–1819. doi:10.3762/bjnano.9.172.

19. Hermes, I. M.; Best, A.; Winkelmann, L.; Mars, J.; Vorpahl, S. M.; Mezger, M.; Collins, L.; Butt, H.-J.; Ginger, D. S.; Koynov, K.; Weber, S. A. L. *Energy Environ. Sci.* **2020**, *13* (11), 4168–4177. doi:10.1039/d0ee01016b.

20. Rohrbeck, P. N. Untersuchung von lokalen Aufladungsdynamiken an Perowskit-Korngrenzen mit zeitaufgelösten KPFM Methoden. Master thesis, Johannes Gutenberg University Mainz, 2021.

21. Bergmann, V. W.; Weber, S. A. L.; Javier Ramos, F.; Nazeeruddin, M. K.; Grätzel, M.; Li, D.; Domanski, A. L.; Lieberwirth, I.; Ahmad, S.; Berger, R. *Nat. Commun.* **2014**, *5* (1), 5001. doi:10.1038/ncomms6001.

22. Weber, S. A. L.; Hermes, I. M.; Turren-Cruz, S.-H.; Gort, C.; Bergmann, V. W.; Gilson, L.; Hagfeldt, A.; Graetzel, M.; Tress, W.; Berger, R. *Energy Environ. Sci.* **2018**, *11* (9), 2404–2413. doi:10.1039/C8EE01447G.

23. Zhu, C.; Fuchs, T.; Weber, S. A. L.; Richter, F. H.; Glasser, G.; Weber, F.; Butt, H.-J.; Janek, J.; Berger, R. *Nat. Commun.* **2023**, *14* (1), 1300. doi:10.1038/s41467-023-36792-7.

24. Martin, Y.; Abraham, D. W.; Wickramasinghe, H. K. *Appl. Phys. Lett.* **1988**, *52* (13), 1103–1105. doi:10.1063/1.99224.

25. Abraham, D. W. *J. Vac. Sci. Technol. B Microelectron. Nanom. Struct.* **1991**, *9* (2), 703. doi:10.1116/1.585536.

26. Garrett, J. L.; Munday, J. N. *Nanotechnology* **2016**, *27* (24), 14. doi:10.1088/0957-4484/27/24/245705.

27. Eaton, P.; West, P. *MRS Bull.*; Oxford University Press, 2010; Vol. 39, pp 379–379. doi:10.1093/acprof:oso/9780199570454.001.0001.

28. Biberger, R.; Benstetter, G.; Goebel, H.; Hofer, A. *Microelectron. Reliab.* **2010**, *50* (9-11), 1511–1513. doi:10.1016/j.microrel.2010.07.052.

29. Lee, D. T.; Pelz, J. P.; Bhushan, B. *Nanotechnology* **2006**, *17* (5), 1484–1491. doi:10.1088/0957-4484/17/5/054.

30. Gomila, G.; Toset, J.; Fumagalli, L. *J. Appl. Phys.* **2008**, *104* (2), 024315. doi:10.1063/1.2957069.

31. Fumagalli, L.; Ferrari, G.; Sampietro, M.; Gomila, G. *Appl. Phys. Lett.* **2007**, *91* (24), 243110. doi:10.1063/1.2821119.

32. Lee, D. T.; Pelz, J. P.; Bhushan, B. *Rev. Sci. Instrum.* **2002**, *73* (10), 3525–3533. doi:10.1063/1.1505655.

33. Kobayashi, K.; Yamada, H.; Matsushige, K. *Appl. Phys. Lett.* **2002**, *81* (14), 2629–2631. doi:10.1063/1.1510582.

34. Kimura, K.; Kobayashi, K.; Yamada, H.; Matsushige, K. *Appl. Surf. Sci.* **2003**, *210* (1-2), 93–98. doi:10.1016/S0169-4332(02)01486-1.

35. Gil, A.; Colchero, J.; G mez Herrero, J.; Bar, A. M. *Nanotechnology* **2003**, *14* (2), 332–340. doi:10.1088/0957-4484/14/2/345.

36. Platz, D.; Tholén, E. A.; Pesen, D.; Haviland, D. B. *Appl. Phys. Lett.* **2008**, *92* (15), 153106. doi:10.1063/1.2909569.

37. Borgani, R.; Forchheimer, D.; Bergqvist, J.; Thorén, P.-A.; Inganäs, O.; Haviland, D. B. *Appl. Phys. Lett.* **2014**, *105* (14), 143113. doi:10.1063/1.4897966.

38. Garrett, J. L.; Leite, M. S.; Munday, J. N. *ACS Appl. Mater. Interfaces* **2018**, *10* (34), 28850–28859. doi:10.1021/acsami.8b08097.

39. Dobryden, I.; Borgani, R.; Rigoni, F.; Ghamgosar, P.; Concina, I.; Almqvist, N.; Vomiero, A. *Nanoscale Adv.* **2021**, *3* (15), 4388–4394. doi:10.1039/D1NA00319D.

40. Crider, P. S.; Majewski, M. R.; Zhang, J.; Oukris, H.; Israeloff, N. E. *Appl. Phys. Lett.* **2007**, *91* (1), 2–5. doi:10.1063/1.2753539.

41. Labardi, M.; Prevosto, D.; Nguyen, K. H.; Capaccioli, S.; Lucchesi, M.; Rolla, P. *J. Vac. Sci. Technol. B, Nanotechnol. Microelectron. Mater. Process. Meas. Phenom.* **2010**, *28* (3), C4D11–C4D17. doi:10.1116/1.3368597.

42. Schwartz, G.; Riedel, C.; Arinero, R.; Tordjeman, P.; Alegría, A.; Colmenero, J. *Ultramicroscopy* **2011**, *111* (8), 1366–1369. doi:10.1016/j.ultramic.2011.05.001.

43. Miccio, L. A.; Kummali, M. M.; Schwartz, G. A.; Alegría, Á.; Colmenero, J. *Ultramicroscopy* **2014**, *146*, 55–61. doi:10.1016/j.ultramic.2014.06.006.

44. Miccio, L. A.; Kummali, M. M.; Schwartz, G. A.; Alegría, Á.; Colmenero, J. *J. Appl. Phys.* **2014**, *115* (18), 184305. doi:10.1063/1.4875836.

45. Miccio, L. A.; Schwartz, G. A. Study of relaxation and transport processes by means of AFM based dielectric spectroscopy. In *AIP Conf. Proc.*; AIP Publishing LLC, 2014; pp 150–153. doi:10.1063/1.4876800.

46. Checa, M.; Neumayer, S. M.; Susner, M. A.; McGuire, M. A.; Maksymovych, P.; Collins, L. *Appl. Phys. Lett.* **2021**, *119* (25), 252905. doi:10.1063/5.0078034.

47. Gramse, G.; Edwards, M. A.; Fumagalli, L.; Gomila, G. *Appl. Phys. Lett.* **2012**, *101* (21), 213108. doi:10.1063/1.4768164.

48. Gramse, G.; Casuso, I.; Toset, J.; Fumagalli, L.; Gomila, G. *Nanotechnology* **2009**, *20* (39), 395702. doi:10.1088/0957-4484/20/39/395702.

49. Hudlet, S.; Saint Jean, M.; Guthmann, C.; Berger, J. *Eur. Phys. J. B* **1998**, *2* (1), 5–10. doi:10.1007/s100510050219.

50. Colchero, J.; Gil, A.; Baró, A. M. *Phys. Rev. B* **2001**, *64* (24), 245403. doi:10.1103/PhysRevB.64.245403.

51. Law, B. M.; Rieutord, F. *Phys. Rev. B* **2002**, *66* (3), 035402. doi:10.1103/PhysRevB.66.035402.

52. Mourran, A.; Tartsch, B.; Gallyamov, M.; Magonov, S.; Lambreva, D.; Ostrovskii, B. I.; Dolbnya, I. P.; de Jeu, W. H.; Moeller, M. *Langmuir* **2005**, *21* (6), 2308–2316. doi:10.1021/la048069y.

53. Magonov, S.; Alexander, J. *Beilstein J. Nanotechnol.* **2011**, *2* (1), 15–27. doi:10.3762/bjnano.2.2.

54. Sader, J. E.; Chon, J. W. M.; Mulvaney, P. *Rev. Sci. Instrum.* **1999**, *70* (10), 3967–3969. doi:10.1063/1.1150021.

55. Labuda, A.; Kocun, M.; Lysy, M.; Walsh, T.; Meinhold, J.; Proksch, T.; Meinhold, W.; Anderson, C.; Proksch, R. *Rev. Sci. Instrum.* **2016**, *87* (7), 073705. doi:10.1063/1.4955122.

56. Reichel, P. Tip-sample capacitance in electrostatic force microscopy. Bachelor thesis, University of Mainz, 2021.